International Journal of Heat and Mass Transfer 55 (2012) 586–596

Contents lists available at SciVerse ScienceDirect

International Journal of Heat and Mass Transfer

journal homepage: www.elsevier.com/locate/ijhmt

Wicking and thermal characteristics of micropillared structures for use in passive heat spreaders

Ram Ranjan, Abhijeet Patel, Suresh V. Garimella *, Jayathi Y. Murthy

Cooling Technologies Research Center, An NSF IUCRC, School of Mechanical Engineering and Birck Nanotechnology Center, Purdue University, 585 Purdue Mall, West Lafayette, IN 47907, USA

ARTICLE INFO

Article history:
Received 3 May 2011
Received in revised form 7 October 2011
Accepted 17 October 2011
Available online 21 November 2011

Keywords:
Heat pipe
Thermal spreaders
Wick structure
Evaporation
Micro-pillars

ABSTRACT

The thermal and hydrodynamic performance of passive two-phase cooling devices such as heat pipes and vapor chambers is limited by the capabilities of the capillary wick structures employed. The desired characteristics of wick microstructures are high permeability, high wicking capability and large extended meniscus area that sustains thin-film evaporation. Choices of scale and porosity of wick structures lead to trade-offs between the desired characteristics. In the present work, models are developed to predict the capillary pressure, permeability and thin-film evaporation rates of various micropillared geometries. Novel wicking geometries such as conical and pyramidal pillars on a surface are proposed which provide high permeability, good thermal contact with the substrate and large thin-film evaporation rates. A comparison between three different micropillared geometries – cylindrical, conical and pyramidal – is presented and compared to the performance of conventional sintered particle wicks. The employment of micropillared wick structure leads to a 10-fold enhancement in the maximum heat transport capability of the device. The present work also demonstrates a basis for reverse-engineering wick microstructures that can provide superior performance in phase-change cooling devices.

© 2011 Elsevier Ltd. All rights reserved.

1. Introduction

Heat spreading and dissipation from microelectronics packages are posing an increasing challenge due to the large heat fluxes encountered. Phase change cooling devices, such as heat pipes and vapor chambers (Fig. 1), can dissipate heat from a small high-flux heat source to a low-flux diffuse area with very low temperature drops [1,2]. These devices contain discrete evaporator and condenser regions for heat input and rejection, respectively, while utilizing a capillary porous medium, also known as the wick structure, to transport the working fluid from the condenser to the evaporator regions by capillary action. The device utilizes the latent heat of the working fluid for achieving high heat transport capability. A major bottleneck in enhancing the thermal performance of the heat pipe is the thermal resistance of the wick [3,4]. At heat fluxes below approximately 100 W/cm^2 and for thickness-constrained packaging applications, the evaporator resistance has been shown to be the most critical component in reducing the thermal resistance of the device [5,6]. The evaporator resistance is comprised of the bulk resistance of the wick material as determined by its thermal conductivity, and the resistance offered by the evaporating liquid meniscus as determined by the thickness of the liquid film near the solid–liquid contact line [7]. The temperature drop across the evaporator, $(T_e - T_v)$, as depicted in Fig. 1 is typically the largest temperature drop in the heat pipe. While the resistance offered by the bulk wick structure in the evaporator section is the limiting resistance in many conventional applications, the meniscus resistance has been shown to be important for very thin (<200 μm) [5] high thermal conductivity wick structures (k > 100 W/mK) [8,9]. Furthermore, the maximum transport capability of a heat pipe (its capillary limit) is determined by the liquid transport in the wick structure. Hence, the device performance may best be improved by optimizing the wick structure. Moreover, the introduction of novel wicking structures with improved liquid transport and thermal performance characteristics is essential for the design of next-generation thermal spreaders.

In recent work, the authors [3,7] studied the wicking and evaporation characteristics of various wick microstructures, *viz.*, sintered particles, screen meshes, rectangular grooves and cylindrical micropillars, and concluded that sintered particle wicks have the best performance characteristics among those considered. They also showed that intense evaporation occurs from a very thin liquid film region (film thickness <10 μm) formed near the solid–liquid contact line in the pore of the wick structure, also known as the thin-film region [10,11]. Wick structures which sustain a larger thin-film area on the liquid meniscus lead to higher rates of evaporation heat transfer [3,7]. While sintered particle wick

* Corresponding author. Tel.: +1 765 494 5621.
E-mail address: sureshg@purdue.edu (S.V. Garimella).

0017-9310/$ - see front matter © 2011 Elsevier Ltd. All rights reserved.
doi:10.1016/j.ijheatmasstransfer.2011.10.053

Nomenclature

A	area
C_P	specific heat
D	diameter of sphere/pillar, base side length of pyramidal pillars
h	height of liquid free surface from bottom surface in the initial configuration
h_b	base heat transfer coefficient
h_{evap}	convection heat transfer coefficient for evaporation
h_{fg}	latent heat of evaporation
h_{nat}	heat transfer coefficient for natural convection
h_l	liquid enthalpy
H	dimensionless height of liquid free surface ($=h/L$)
k	thermal conductivity
K	permeability
l	height of the pillars
L	characteristic length ($=r=d/2$)
$\dot{m}''$	evaporative mass flux
$\overline{M}$	molecular weight
Nu	Nusselt number ($h_{\text{nat}}L/k$)
p'	pitch
P'	non-dimensional pitch (p'/L)
p, P	hydrodynamic pressure
ΔP_c	capillary pressure
Pr	Prandtl number
$\dot{q}$	heat transfer rate
r	radius of pillars/spheres
r_p	pore radius
R	universal gas constant
Ra	Rayleigh number ($=(g\beta\lvert T_{\text{wall}}-T_v\rvert d^3 Pr)/\nu^2$)
Re	Reynolds number ($=\rho dV/\mu$)
S_M	mass source term
T	temperature
V	velocity/volume

Greek Symbols

α	thermal diffusivity
β	thermal expansion coefficient
δ_0	non-evaporating thin-film thickness
δ	thin-film thickness
ε	wick porosity
σ	surface tension between liquid and vapor phases
ρ	density of liquid
θ	contact angle between liquid and solid surface
ν	kinematic viscosity
μ	dynamic viscosity
$\hat{\sigma}$	accommodation coefficient

Subscripts

b	base substrate area in evaporation model
bot	bottom solid wall
cell	cell element
e	evaporator
equ	equilibrium
f	face of cell element
l	liquid
lv	liquid–vapor interface
max	maximum
mic	micro-region of the meniscus
sat	saturation
ref	reference
v	vapor
wall	non-wet portion of the solid wall

structures have been shown to have good wicking and thin-film evaporation characteristics, their bulk thermal conductivity (~40 W/mK [12]) is lower than that of recently explored micropillared geometries [13–15] for heat pipes.

Micropillared wicks have been investigated for lab-on-a-chip [16], biomedical [17] and thermal management [14] applications. Pillar structures may be used in microchannels to increase the surface/volume ratio and to increase capillary flow [18]. Xiao et al. [15] presented an experimentally-validated semi-analytical model for predicting the rate of propagation of a liquid through micropillar arrays. They used the software SURFACE EVOLVER [19] to compute the shape of the liquid meniscus in a unit cell of the micropillar array. The meniscus shape was utilized to obtain correlations for the liquid volume filling the microstructure as well as the meniscus area for a given pillar diameter and pitch. Ding et al. [13] fabricated titanium micropillars and studied the wetting behavior of the pillars using numerical and experimental techniques. Advanced photolithography techniques have enabled the fabrication of novel micropillared structures which can decrease the evaporator resistance and improve heat pipe performance. In

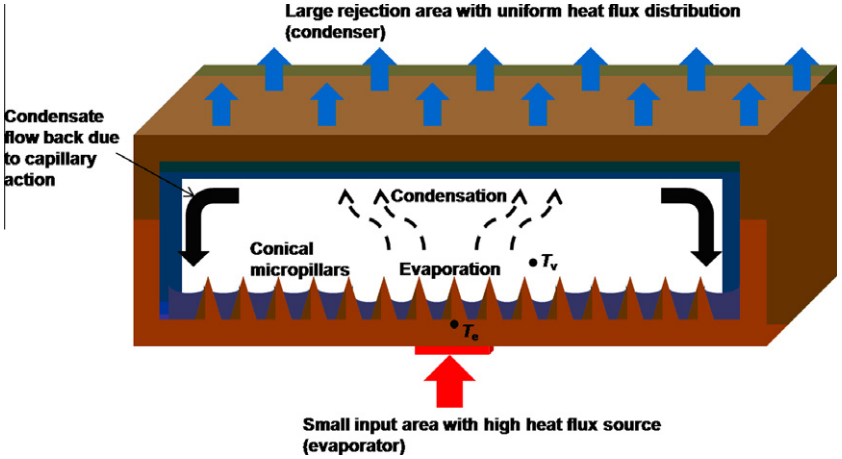

Fig. 1. Schematic of a flat heat pipe (vapor chamber).

comparison to grooved and sintered particle wick structures, micropillar wick structures may have the following advantages:

(1) Micropillared wicks possess higher thermal conductivity as compared to sintered particle wick structures since they can be grown or micro-machined on the substrate itself. At lower heat inputs, when the wick offers the limiting thermal resistance in a heat pipe [6,20], micropillar surfaces are expected to lead to a better performance.
(2) Micropillar wick structures exhibit high permeability and may lead to smaller liquid pressure drop, thus increasing the maximum heat transport capability of the device.

In the present work, various micropillared geometries are compared for their performance in heat pipes or thermal spreaders. Models are developed for computing the capillary pressure and permeability of these wick structures. Thin-film evaporation from the liquid menisci formed in the wick pores is computed using kinetic theory [21]. The performance of different microstructures is compared at a fixed porosity and permeability. The pillar geometry which leads to the generation of the highest capillary pressure and maximum thin-film evaporation rate is identified. Finally, the best performing micropillar geometry is compared with a commercial sintered particle wick structure.

2. Problem description

2.1. Microstructure topologies

The microstructures considered in the present work are shown in Fig. 2. Conical, cylindrical and pyramidal micropillar shapes are considered, as shown in Fig. 2(a)–(c), respectively. The pillars are assumed to be in a square-packing arrangement. Such an arrangement is commonly used in the fabrication of microstructures [13–15]. The performance characteristics of these micropillared geometries is compared with that of a sintered particle wick structure, shown as uniform spheres in a square-packed arrangement on a surface [3] in Fig. 2(d).

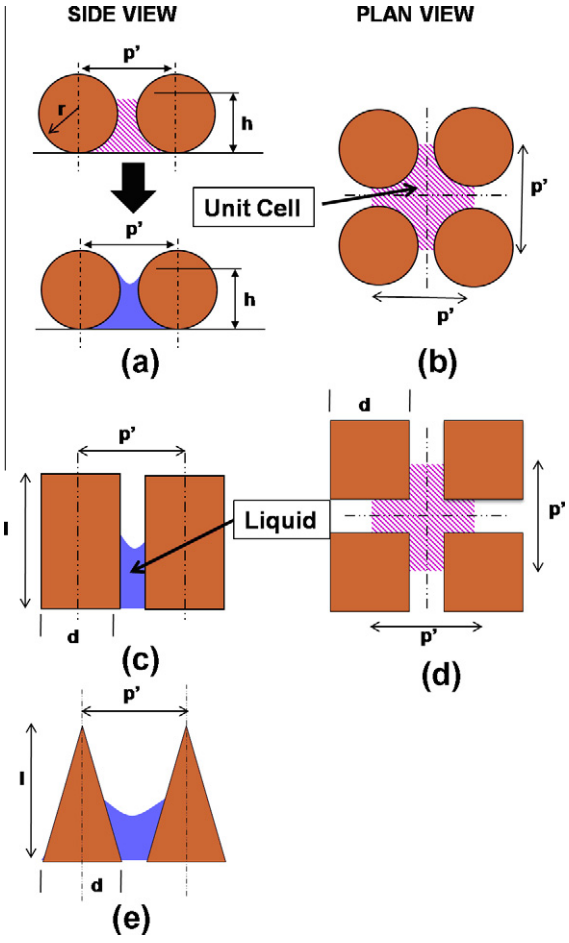

Fig. 3. Side views of the surfaces with square-packed (a) spheres, (c) cylindrical pillars, and (e) conical and pyramidal pillars. Plan views of the surface are also shown for (b) spheres, cylindrical and conical pillars and (d) pyramidal pillars. The corresponding unit cell is also shown in each case.

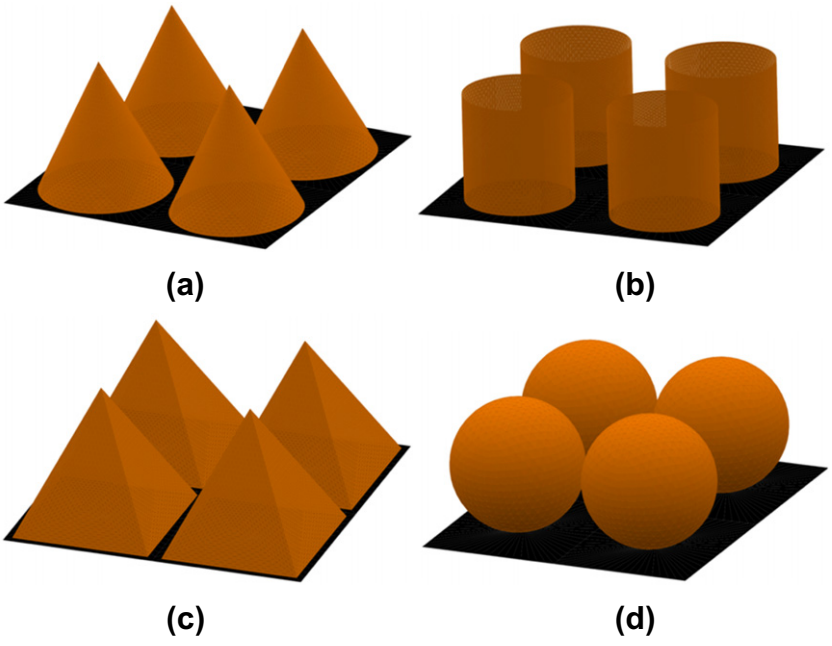

Fig. 2. Schematic representations of the micropillared geometries considered: (a) conical, (b) cylindrical, and (c) pyramidal. Also shown is (d) a sintered particle bed modeled as uniform spheres on a surface. Each geometry is modeled in the square-packed configuration.

Only the repetitive unit cells representing the microstructures are modeled, as presented previously [3] by the authors. The unit cells for the four surfaces are shown in Fig. 3 and described below.

Topology 1: Uniform conical pillars on a surface in a square packing arrangement (Fig. 3(b) and (e)).
Topology 2: Uniform cylindrical pillars on a surface in a square packing arrangement (Fig. 3(c) and (b)).
Topology 3: Uniform pyramidal pillars on a surface in a square packing arrangement (Fig. 3(e) and (d)).
Topology 4: Uniform spherical particles on a surface in a square packing arrangement (Fig. 3(a) and (b)).

In Fig. 3(a), h is the initial height of the filling liquid measured from the bottom, and r is the radius of the spheres/pillars. The pitch, p', is defined as the distance between the centers of adjacent spheres/pillars. The pitch is assumed to be the same in both the longitudinal and transverse directions in all the four geometries. The non-dimensional pitch, P', is given by p'/r. In Fig. 3(c)–(e), d is the diameter of the pillars or the side length of the pyramids. d is taken to be $2r$ for all the pillared structures while the liquid level in the wick pore, h, is varied from $0.2r$ to r. The liquid level in the wick pore of a heat pipe depends on various factors such as input heat flux and fluid charge, a comparison of capillary pressure generated by different wick structures is presented over a range of liquid levels in the pore. The height of the conical, cylindrical and pyramidal pillars, l, is equal to the diameter of the pillars. The unit cells shown in Fig. 3 are considered for modeling the performance of the four geometries. The porosity is defined as the ratio of void volume to the total volume of the unit cell. The performance of the four structures is compared for fixed values of the wick porosity and permeability.

2.2. Performance parameters

The parameters which characterize the performance of a microstructure in a heat pipe are its capillary pressure, permeability, thermal conductivity, and the rate of thin-film evaporation from the liquid meniscus formed in its pore. While only thin-film evaporation occurs in the wick structure at low heat inputs, nucleate boiling can occur in the wick structure at high heat flux inputs (>100 W/cm^2) [4,5] which leads to a decrease in the wick's thermal resistance. In this study, incipience of boiling is not considered as a performance parameter. Hence, the comparison of performance of the microstructures is based on their capillary pressure, permeability, thermal conductivity and thin-film evaporation, as described below:

2.2.1. Permeability and capillary pressure

The ideal microstructure must provide high capillary pressure in the evaporator region of the heat pipe so that the return of the liquid from the condenser to evaporator regions is ensured even at high heat inputs. To avoid dry-out of the evaporator region, the available capillary pressure in the evaporator region (Δp_c) must compensate for the flow pressure drops in the wick (Δp_l) and vapor (Δp_v) regions. This can be represented as the following condition:

$$\Delta p_c \geqslant \Delta p_l + \Delta p_v \tag{1}$$

The available capillary pressure (Δp_c) in the heat pipe is determined by the pore radius in the evaporator region, assuming that the meniscus has an infinite radius of curvature in the condenser region, i.e.,

$$\Delta p_c = \frac{2\sigma_{lv}}{r_p} \tag{2}$$

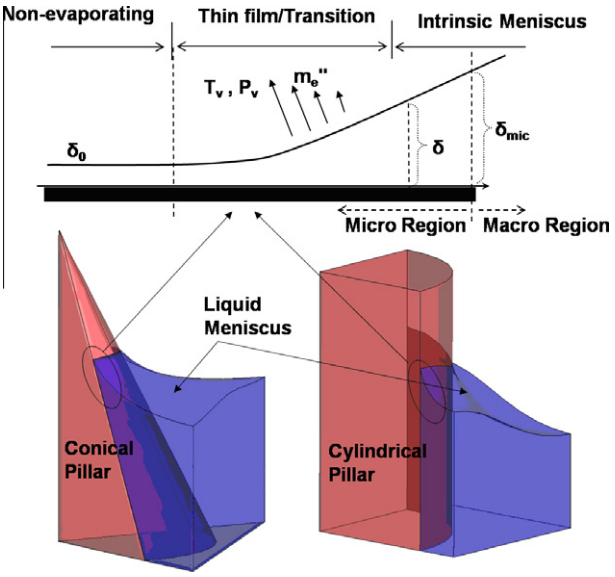

Fig. 4. Schematic diagrams showing the formation of thin liquid films near the solid–liquid contact lines of the liquid meniscus.

where σ_{lv} is the surface tension of the liquid-vapor interface and r_p is the pore radius. Thus, smaller pore radii lead to the generation of higher capillary pressure. However, the permeability of the wick structure diminishes as the pore radius decreases, thus increasing the flow pressure drop, Δp_l, in the wick structure.

2.2.2. Thermal conductivity and thin-film evaporation

A model which computes the combined thermal resistance offered by the wick structure and the liquid meniscus formed in the wick pore has been developed. The thin-film region of the liquid meniscus, formed near the solid–liquid–vapor contact line, characterizes the evaporative heat transfer rate of the meniscus under the given wall superheat and saturated vapor conditions [7]. The contact line region of the liquid meniscus, as shown in Fig. 4, consists of the non-evaporating thin-film region where intermolecular forces such as van der Waals forces and disjoining pressure [10] are predominant. The thin-film region of the liquid meniscus, also known as the transition region, is defined as the region between the non-evaporating film and the intrinsic meniscus. The authors have previously [7] shown that the thin-film region, defined as the region in which the film thickness (δ) is below 10 μm (δ_{mic}), accounts for more than 80% of the total heat transfer. The enhancement of the thin-film area in the liquid meniscus will lead to increased evaporation rates. Fig. 4 shows the thin-film regions of the liquid menisci for the cases of conical and cylindrical pillars. The solid surface in the case of the conical pillar has greater proximity to the liquid-free surface due to its slope, as compared to that in the case of the cylindrical pillar.

In previous work [3,7], different wick microstructures were compared for their wicking and thin-film evaporation performance while the porosity and the length scale were kept the same for all the structures. In this study, two different cases are considered. In one case, a fixed porosity is assigned to the microstructures while in the other case, the permeability of the microstructures is kept the same. Keeping the permeability the same ensures that the microstructures have the same pressure drop (Δp_l) for a given liquid mass flow rate. The wicking and thin-film evaporation performance of different structures are then compared to identify the best performing microstructure.

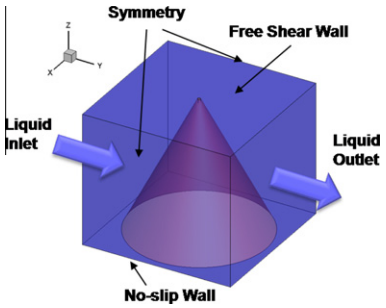

Fig. 5. Unit cell and boundary conditions for the computation of permeability for a microstructure composed of square-packed conical pillars.

3. Numerical method

This section describes the various numerical models developed in this study to predict the performance of microstructures under the given geometric and boundary conditions. The models for computing the permeability and capillarity are presented, followed by a description of the thin-film evaporation model.

3.1. Permeability model

Since established correlations for the permeability of micropillars on a substrate are not available in the literature, the liquid flow across the pillars is computed using FLUENT®, a finite-volume based flow solver [22]. Low-Reynolds number flow with $Re = 0.1$ is modeled for conical, cylindrical and pyramidal pillars on a substrate. The value of 0.1 for Re is chosen based on typical flow velocities encountered in the wick structure of vapor chambers. The flow velocity in the wick structure is of the order of 10^{-4} m/s for a 3 mm thick vapor chamber with a 0.2 mm thick wick structure [8]. Based on this flow velocity, the Reynolds number in the wick structure is 0.1 ($Re = \rho u L/\mu$ where $\rho = 1000$ kg/m^3, $\mu = 0.001$ Ns/m^2 for water and $u = 10^{-4}$ m/s, $L = 1$ mm as wick length scale). Three-dimensional models with unit-cell representations of the micropillared geometries are developed. Such a model for the case of conical pillars, along with the corresponding flow boundary conditions, is shown in Fig. 5. A periodic flow condition is used at the liquid inlet and outlet boundaries. Symmetry conditions are applied at the transverse boundaries while a free shear condition is prescribed at the top boundary. The height of the domain is taken to be the same as the pillar height in every case. The permeability (K) is obtained using Darcy's law [23]

$$\nabla p = -\frac{\mu \dot{m}}{KA\rho} \tag{3}$$

in which A is the flow cross-sectional area and $\dot{m}$ is the liquid mass flow rate. A typical grid used for the permeability computations has 500,000 tetrahedral elements. The permeability changed by less than 1.5% if a higher grid size was used (with 3,000,000 elements), thus indicating that the computational results were independent of the grid size. The permeability of various micropillared geometries is computed as a function of the wick porosity. The porosity (ε) and permeability (K) for all four microstructures are presented in Table 1; the correlations for the permeability of micropillared geometries as a function of porosity and pillar radius are obtained using the least-squares curve-fit feature of MATLAB [24].

Table 1
Porosity and permeability of the microstructures.

Structure	Porosity	Permeability
Cylindrical	$\varepsilon = 1 - \frac{\pi}{4p'^2}$	$K = \frac{27.6r^2\varepsilon^{8.43}}{(1-\varepsilon)^{-2.88}}$
Conical	$\varepsilon = 1 - \frac{\pi}{12p'^2}$	$K = \frac{0.0964r^2\varepsilon^{3.55}}{(1-\varepsilon)^{0.6}}$
Pyramidal	$\varepsilon = 1 - \frac{1}{3p'^2}$	$K = \frac{9.3\times10^4 r^2\varepsilon^{27.4}}{(1-\varepsilon)^{-4.55}}$
Spheres [1]	$\varepsilon = 1 - \frac{\pi}{6p'^2}$	$K = \frac{4r^2\varepsilon^3}{150(1-\varepsilon)^2}$

3.2. Capillary pressure model

The capillary pressure Δp_c generated by a wick depends on the mean curvature of the liquid meniscus H formed in its pore and the surface tension σ_{lv} of the liquid, as given by the Young–Laplace equation [25]:

$$\Delta p_c = \sigma_{lv}\left(\frac{1}{r_1} + \frac{1}{r_2}\right) = 2H\sigma_{lv} \tag{4}$$

where Δp_c is the capillary pressure defined as $(p_l - p_v)$, and r_1, r_2 are any two orthogonal radii of curvature at a point on the meniscus. Δp_c is non-dimensionalized as $\Delta P_c = \Delta p_c L/\sigma_{lv}$. The characteristic length, L, is taken as the radius of the particles/pillars. The mean curvature of the liquid meniscus in a wick pore is computed under prescribed constraints (liquid volume, contact angle) using the surface energy minimization program, SURFACE EVOLVER [19]. Based on the meniscus curvature, the capillary pressure is calculated using Eq. (4). The meniscus shape depends on the geometry (pillar/particle diameter, wick porosity), the liquid level in the wick pore and the solid–liquid contact angle. The details of this model may be found in previous work by the authors [3].

3.3. Thin-film evaporation model

The combined resistance of the wick structure and the liquid meniscus formed in the wick pore is computed numerically using an evaporating meniscus model [7] developed previously. The computational domain and boundary conditions for the case of conical pillars are shown in Fig. 6. Incompressible, laminar and steady flow of water with constant properties is assumed in the liquid domain. The vapor domain is assumed to be saturated at a given temperature and the flow field is not solved in the vapor domain. The following continuity, momentum and energy equations are solved in the liquid domain:

$$\nabla.\vec{V} = 0 \tag{5}$$

0

(6)

(7)

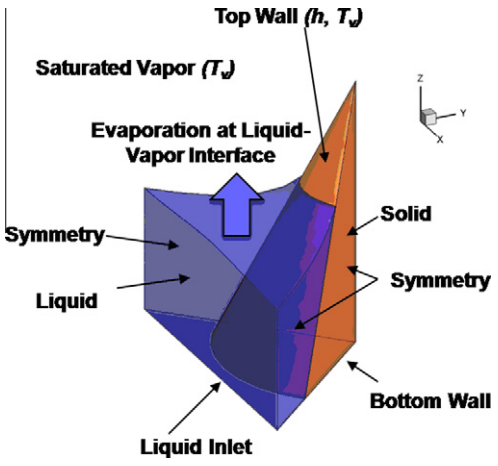

Fig. 6. Unit cell and boundary conditions for the computation of evaporation rate from a liquid meniscus formed in the pore between conical pillars, $\theta = 5°$, $\varepsilon = 78\%$.

In the solid wall, the energy equation reduces to:

$$\nabla^2 T = 0 \tag{8}$$

In Fig. 6, the incoming liquid is assumed to be at a constant temperature, T_{inlet}, with a stagnation-pressure inlet boundary condition [22]. A constant temperature boundary condition is applied at the bottom solid wall. The bottom wall represents the base area of the pillar on the substrate wall. In the case of the sintered wick structure, the bottom wall is assumed to have a contact area diameter of 0.1 d (brought about in practice by sintering of the spheres to the base). The temperature of the bottom wall is represented by T_{bot}. A convective heat transfer boundary condition is imposed on the non-wetted portion of the pillars/spheres exposed to vapor labeled *Top Wall* in Fig. 6. For this portion of the boundary, we have

$$-k_{\text{wall}} \nabla T.\vec{n} = h_{\text{nat}}(T_{\text{wall}} - T_v) \tag{9}$$

The value of the natural convection coefficient h_{nat} on the surface of spheres and pillars is given by:

$$h_{\text{nat}} = \frac{k}{d} Nu \tag{10}$$

in which the Nusselt number, Nu, is calculated as [26]:

$$Nu = \left(0.6 + \frac{0.387 Ra^{1/6}}{(1 + (0.559/Pr)^{9/16})^{8/27}}\right)^2 \tag{11}$$

$$Ra = (g\beta |T_{\text{wall}} - T_v| d^3 Pr)/\nu^2 \tag{12}$$

For a pillar of diameter = 200 μm and $T_{\text{wall}} - T_v$ = 2.5 K, $h_{\text{nat}} \approx 38$ W/m^2 K. This value of h_{nat} is used for all microstructures in the present work.

The evaporation rate at the liquid-vapor interface in the wick pore is computed for a given wall superheat under saturated vapor conditions using the relation given by Schrage [21]. The liquid–vapor interface is modeled as a fixed interface with a convective boundary condition; h_{evap} is obtained using the evaporative mass flux expression:

$$\dot{m}'' = \frac{2\hat{\sigma}}{2 - \hat{\sigma}} \left(\frac{\overline{M}}{2\pi \overline{R}}\right)^{1/2} \left(\frac{p_{v\_equ}(T_{lv})}{T_{lv}^{1/2}} - \frac{p_v}{T_v^{1/2}}\right) \tag{13}$$

The value of accommodation coefficient $\hat{\sigma}$ is taken as unity [7,27]. The equilibrium vapor pressure can be approximated as the corresponding saturation pressure, $p_{v\_equ}(T_{lv}) = p_{\text{sat}}(T_{lv})$, which in turn is given by

$$p_{\text{sat}}(T_{lv}) = p_{\text{sat\_ref}} \exp\left(\frac{\overline{M} h_{fg}}{\overline{R}} \left(\frac{1}{T_{\text{sat\_ref}}} - \frac{1}{T_{lv}}\right)\right) \tag{14}$$

The numerical solution is obtained using the pressure-based finite volume scheme in FLUENT [22]. A second-order differencing scheme is used. Pressure–velocity coupling is achieved using the SIMPLE algorithm. Mass transport due to evaporation at the liquid–vapor interface is implemented by imposing mass source terms in the liquid cells adjacent to the interface. This mass source term has a negative value and is given by:

$$S_M = -\dot{m}'' A_f / V_{cell} \tag{15}$$

where A_f is the interface area of the cell and V_{cell} is the volume of the cell. The evaporative heat transfer corresponding to the evaporation rate in Eq. (13) is implemented as an effective convective heat transfer condition at the liquid–vapor interface, with a convective heat transfer rate given by

$$h_{evap} = \frac{\dot{m}'' h_{fg}}{(T_{lv} - T_v)} \tag{16}$$

This ensures that evaporative heat loss $\dot{m}'' h_{fg}$ occurs from the liquid at the liquid-vapor interface.

Grids for all microstructures considered are generated using tetrahedral elements. Only the unit cell representations shown in Fig. 3 are modeled. A water–copper combination is considered in all the simulations. Thermophysical properties of water are listed in Table 2. The details of the model development and validation may be found in the previous work [7] by the authors.

Table 2
Thermophysical properties of water at 298 K.

Fluid	Water
$\overline{M}$ (kg/kmol)	18.01
ρ (kg/m^3)	998.2
k (W/m K)	0.6
μ (kg/ms)	0.00103
C_P (J/kg K)	4181.3
h_{fg} (kJ/kg)	2270×10^3
$d\sigma/dT$ (N/m K)	-15×10^{-5}

4. Results and discussion

The results obtained for the case of conical pillars are discussed in this section. The discussion is followed by a comparison of all the micropillared geometries for their wicking and thin-film evaporation performance. Finally, the best performing micropillared

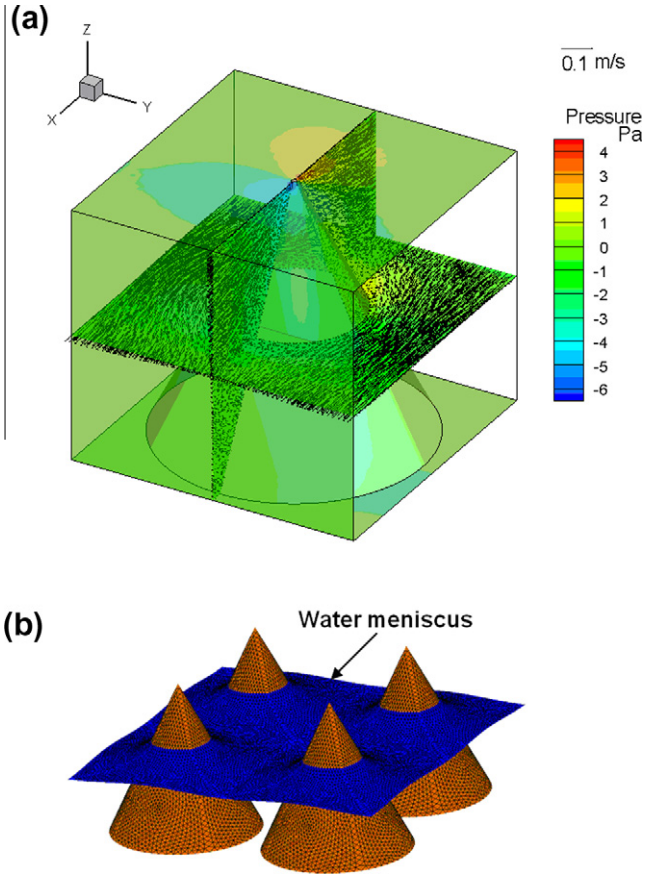

Fig. 7. (a) Pressure (Pa) contours and velocity vectors on the horizontal and vertical planes in the unit cell for permeability computation with conical pillars (P' = 2.2, r = 100 μm); (b) water meniscus formed in the pore between conical pillars (P' = 2.2, r = 100 μm, θ = 5°).

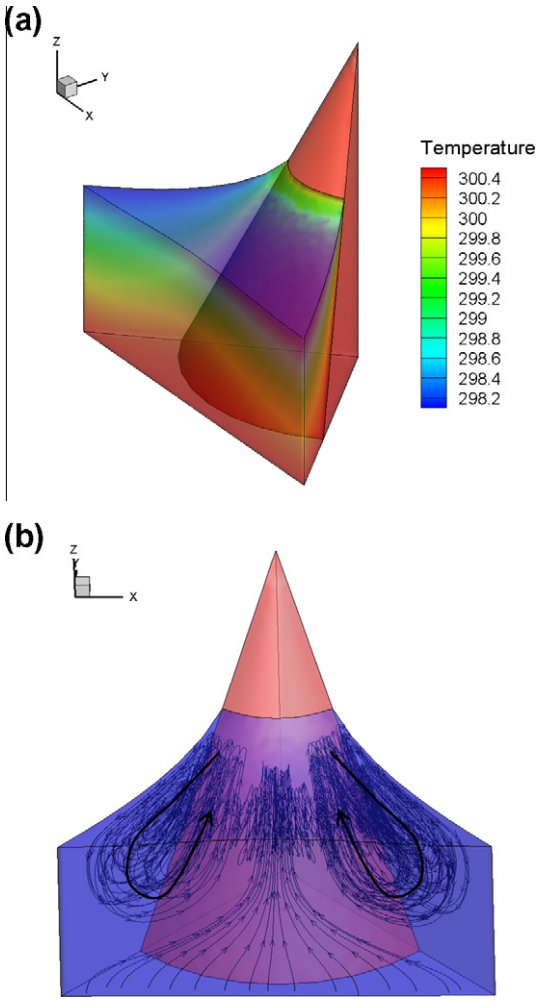

Fig. 8. (a) Temperature contours (K) and (b) Marangoni vortices during thin-film evaporation from the conical pillars (P' = 2.2, r = 100 μm, θ = 5°).

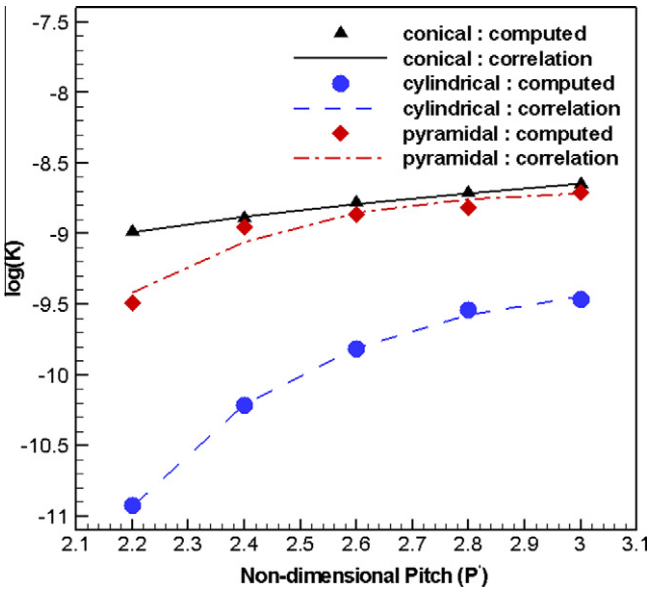

Fig. 9. Permeability of conical, cylindrical and pyramidal pillars as functions of the pitch.

geometry is compared with a commercially-used sintered particle wick structure for its performance as a heat pipe wick.

4.1. Representative characteristics

Fig. 7(a) shows the velocity vectors and pressure contours on the horizontal and vertical mid-planes of the computational domain (see Fig. 5), obtained from the permeability model for the conical pillars. The radius of the pillars is 100 μm while the nondimensional pitch (P') is taken as 2.2, corresponding to the porosity (ε) of 78%. The pressure levels shown are not absolute, and represent the pressure gradient in the flow. It can be inferred from the velocity vectors that most of the liquid flow occurs through the upper (open) portion of the domain which offers a smaller flow resistance. Fig. 7(b) shows the shape of the liquid meniscus for P' = 2.2 and θ = 5°. The meniscus is seen to be puckered, exhibiting anticlastic curvature in the narrow spaces between two adjacent pillars. Using the computed curvature of the liquid meniscus, the capillary pressure is computed as a function of the solid-liquid contact angle and porosity using Eq. (4). The liquid level in the wick pore is varied from 0.2r to r to obtain the maximum capillary pressure generated by the structure irrespective of the liquid level.

The rate of evaporation from the liquid meniscus for a given wall superheat ($T_{bot} - T_v$ = 2.5 K) and a vapor temperature (T_v) of 298 K is obtained as a function of the porosity and solid-liquid contact angle using the thin-film evaporation model. Fig. 8(a) shows the steady-state temperature field on the boundaries of the liquid and solid domains during evaporation from a static meniscus in the pore between square-packed conical pillars. Results are shown for r = 100 μm, p' = 220 μm, θ = 5° and $h = r$. From the temperature contours, it is observed that the evaporation at the liquid–vapor interface leads to cooling of the liquid near the interface relative to the incoming liquid at the inlet. Liquid is fed steadily to the interface to sustain evaporation. The liquid–vapor interface is at the vapor temperature except in the contact line thin-film region. Also, more than 80% of the total evaporation from the interface occurs from approximately 20% of the total area of the meniscus, identified as the thin-film area. The corner region is seen to be at a higher temperature than the central meniscus region which is almost at the vapor temperature. Such non-isothermal evaporation causes thermocapillary stress along the interface, and leads to the formation of Marangoni vortices. A complex toroidal-shaped Marangoni vortex is formed below the interface. As noted in our previous work [7], Marangoni convection leads to less than a 5% increase in the evaporation rate from the meniscus for superheats below 5 K. Thus, Marangoni convection is not relevant for heat transfer in the wick pores of heat pipes where superheats are generally much smaller than 5 K.

4.2. Performance comparison

The permeability, capillary pressure and thin-film evaporation characteristics of different geometries are compared in this section. The three micropillared structures are first compared for their permeability, capillary pressure and thin-film evaporation rates. This is followed by a performance comparison of the best performing micropillar structure with sintered particle wick structure.

4.2.1. Pressure drop

Fig. 9 shows the variation of permeability ($\log(K)$) with respect to the non-dimensional pitch (P') for the conical, cylindrical and pyramidal pillars. The radius is taken as 100 μm for the conical and cylindrical pillars while the base side length of the pyramid is 200 μm. The computed values are plotted along with the values

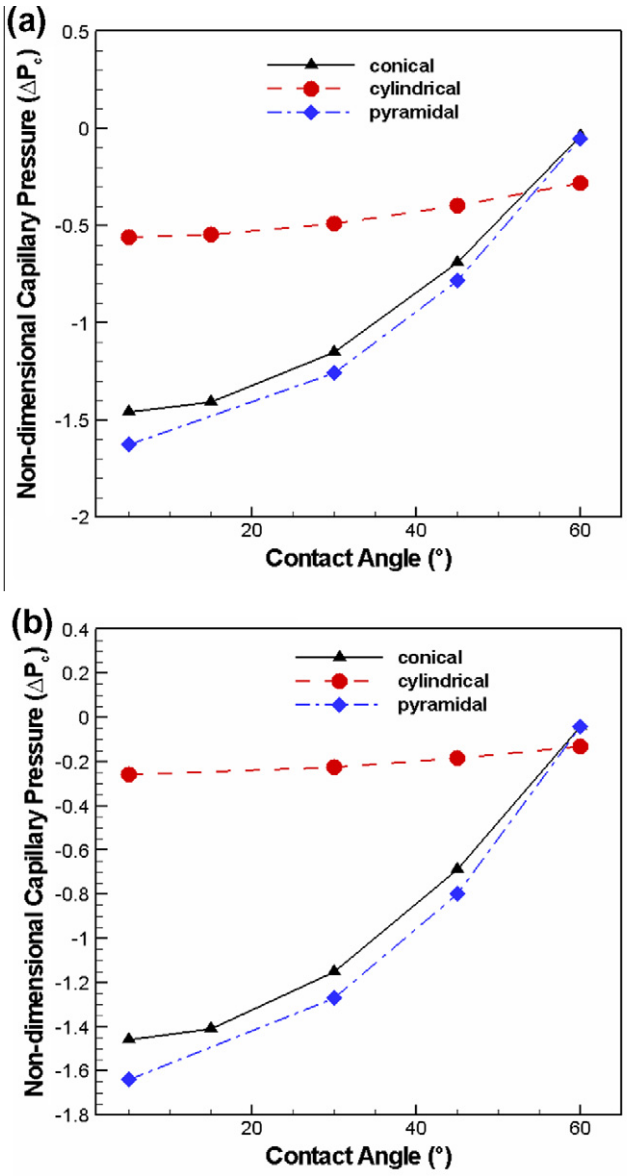

Fig. 10. Non-dimensional capillary pressure as a function of the solid–liquid contact angle for conical, cylindrical and pyramidal pillars for (a) constant porosity, $\varepsilon = 0.78$, and (b) constant permeability, $K = 1.02 \times 10^{-9}$ m^2.

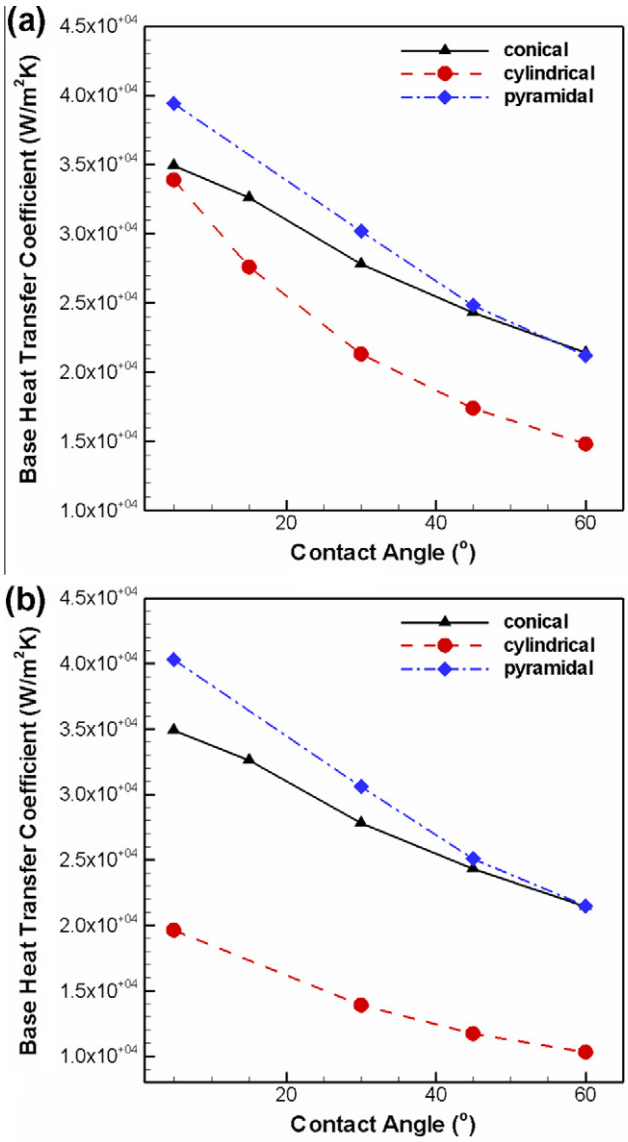

Fig. 11. Base heat transfer coefficient, representing the evaporation rate, as a function of the solid–liquid contact angle for conical, cylindrical and pyramidal pillars for (a) constant porosity, $\varepsilon = 0.78$, and (b) constant permeability, $K = 1.02 \times 10^{-9}$ m^2 ($T_{bot} - T_v$) = 2.5 K, T_{inlet} = 300.5 K, T_v = 298 K, r = 100 μm, $h = r$.

obtained from the correlations (Table 1) derived by curve-fitting. The permeability values are presented for different values of the non-dimensional pitch (P'). The variation in pitch from 1.1 to 1.5 corresponds to a variation in the porosity from 78% to 88%, 35% to 65% and 72% to 85% for the conical, cylindrical and pyramidal pillars, respectively. The value of permeability for the cylindrical pillars is about 2 orders smaller than that for the conical or pyramidal pillars for the smallest pitch (220 μm). The conical and pyramidal pillars have similar permeability at all values of the pitch except at pitches less than ~260 μm. For $p' < 260$ μm, the conical pillars lead to a smaller flow pressure drop than the pyramidal pillars. This can be attributed to the streamlined shape of the conical pillars. This study reveals that the conical and pyramidal pillars lead to a much smaller pressure drop than cylindrical ones for a given liquid mass flow rate. Also, the pillared geometries lead to a much higher permeability than the conventional sintered particle wick structures ($O\ 10^{-10}$ m^2).

4.2.2. Wicking

The maximum non-dimensional capillary pressure ($\Delta P_c = \Delta p_c r/\sigma_{lv}$) is compared for various geometries at different solid–liquid contact angles for the cases of fixed porosity and fixed permeability. Fig. 10(a) shows the variation of ΔP_c with respect to the contact angle θ for $\varepsilon = 78\%$. This porosity corresponds to a pitch of 220 μm, 378 μm and 246 μm for the conical, cylindrical and pyramidal pillars, respectively. The shape of the liquid meniscus is independent of the liquid level h in the case of cylindrical pillars, unlike for the conical and pyramidal pillars. Thus, the capillary pressure generated by the liquid meniscus is independent of the liquid level for the case of the cylindrical pillars. h is taken as r for the cylindrical pillars while it is chosen to be $0.2r$ for the conical and pyramidal pillars. $h = 0.2r$ leads to the generation of the highest capillary pressure at any contact angle for the conical and pyramidal pillars, where the range of variation for h is from $0.2r$ to r. For $0° < \theta < 50°$, the highest capillary pressure is generated with pyramidal pillars. The cylindrical pillars lead to the generation of the least capillary pressure ($|\Delta P_c|$) for $0° < \theta < 50°$. For $\theta > 60°$, the

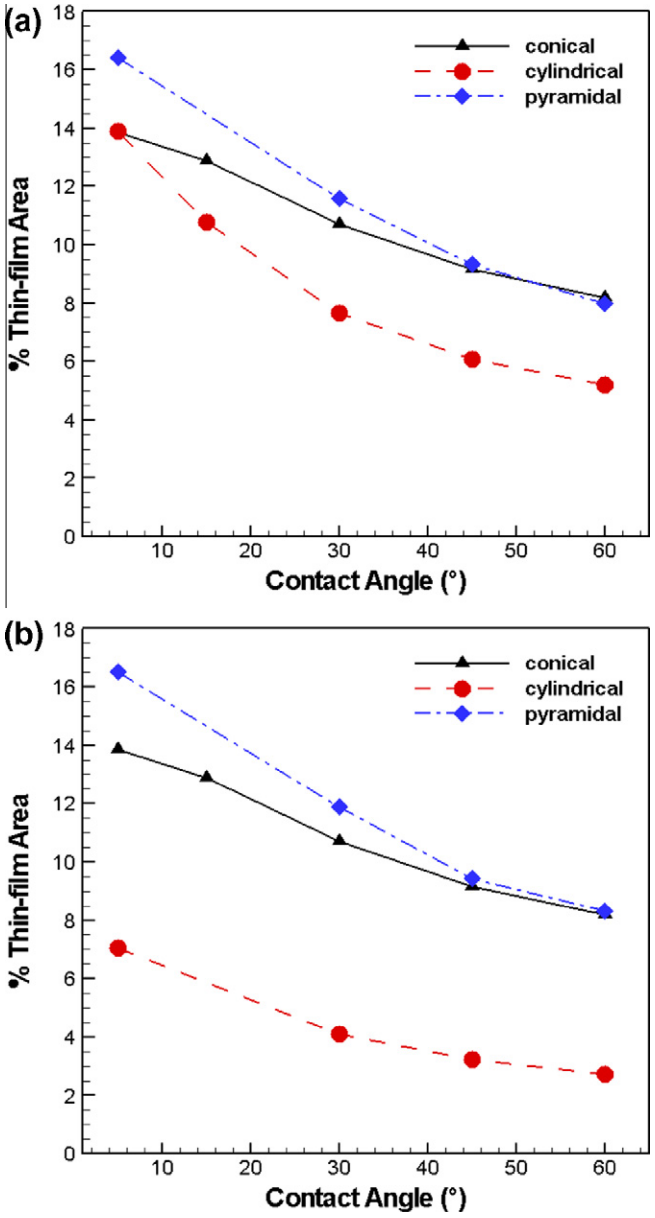

Fig. 12. Percentage thin-film area of the liquid meniscus (total thin-film area per unit base area) as a function of the solid–liquid contact angle for conical, cylindrical and pyramidal pillars for (a) constant porosity, $\varepsilon = 0.78$, and (b) constant permeability, $K = 1.02 \times 10^{-9}$ m^2.

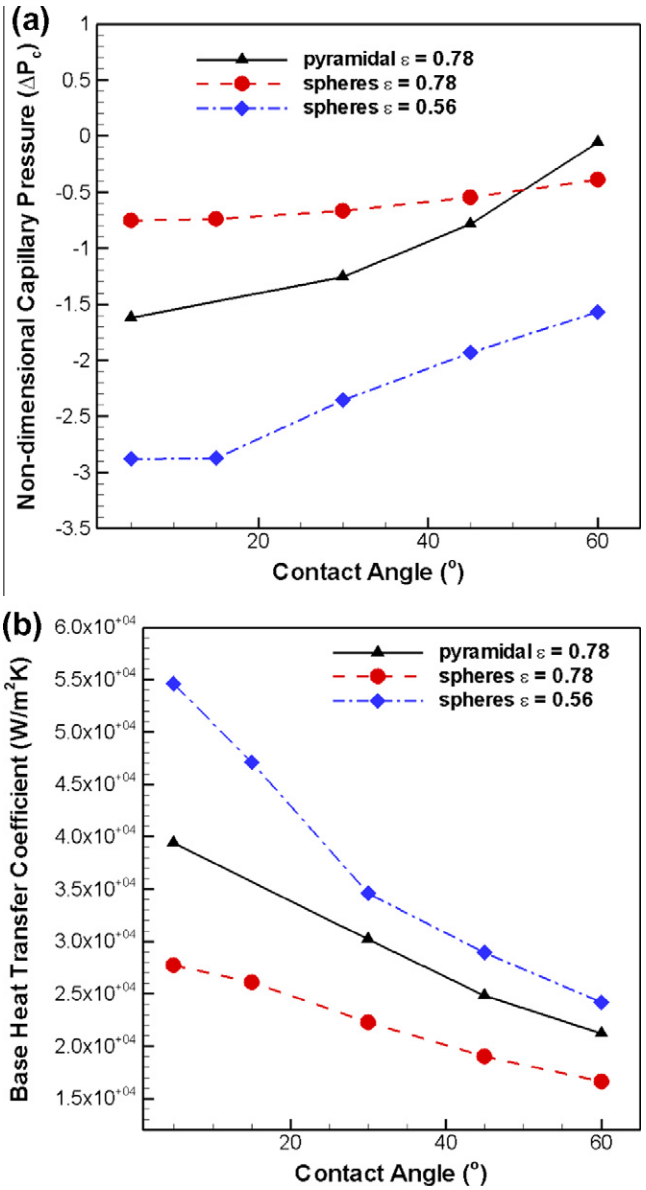

Fig. 13. (a) Non-dimensional capillary pressure, and (b) base heat transfer coefficient as functions of the solid–liquid contact angle for pyramidal pillars and sintered particle wick structures, $(T_{bot} - T_v) = 2.5$ K, $T_{inlet} = 300.5$ K, $T_v = 298$ K, $r = 100$ μm, $h = r$.

menisci formed with conical and pyramidal pillars lead to the generation of positive capillary pressure which is undesirable in the evaporator section of a heat pipe. Hence, θ has been varied only from 0° to 60° for all the cases in this study. Fig. 10(b) shows the variation in ΔP_c with respect to θ for a fixed value of permeability, $K = 1.02 \times 10^{-9}$ m^2. This value of permeability corresponds to a pitch of 220 μm, 522 μm and 244 μm and porosities of 78%, 88.5% and 77.6% for the conical, cylindrical and pyramidal pillars, respectively. Again, the capillary pressure generated in the case of pyramidal pillars is the highest among all the three pillared geometries.

4.2.3. Evaporation from liquid meniscus

The rate of evaporation from the liquid menisci formed in the pores of the three pillared geometries are computed for different contact angles and a solid superheat $(T_{bot} - T_v)$ of 2.5 K with $T_{inlet} = 300.5$ K and $T_v = 298$ K. The net heat transfer rate from the base area of the unit cell is utilized to obtain the base heat transfer coefficient $(h_b = (\dot{q}_{bot} + \dot{q}_{inlet})/(A_b(T_{bot} - T_v)))$. The liquid level h in the wick pores is taken as the pillar radius r (=100 μm) for all cases. This is based on a previous study [7] by the authors where they showed that the liquid level in the wick pore leads to a variation of less than 5% in the rate of evaporation from the liquid meniscus. Fig. 11(a) shows the variation of base heat transfer

Table 3
Comparison of the permeability of the sintered particle and pyramidal micropillared structures at different porosities.

Structure	Porosity (ε)	Pitch (p')	K (m^2)
Sintered particle wick	0.56	220	2.42×10^{-10}
	0.78	308	2.61×10^{-9}
Pyramidal micropillars	0.78	246	1.04×10^{-9}

Table 4
Performance comparison between pyramidal micropillars and sintered particle wick structure.

Case of comparison	Performance remarks	
	Capillary limit (maximum heat transport capability)	Base heat transfer coefficient
Pyramidal micropillars (ε = 78%) vs. sintered particles (ε = 78%)	Similar	1.5 times improvement in h_b due to micropillars
Pyramidal micropillars (ε = 78%) vs. sintered particles (ε = 56%)	10 times improvement in capillary limit due to micropillars	1.3 times lower h_b due to micropillars

coefficient with contact angle for the different geometries for a fixed wick porosity of 78%. The base heat transfer coefficient represents the total heat transfer from the base area of the unit cell normalized by the combined area of the liquid inlet and the bottom wall (Fig. 6). The variation in heat transfer coefficient with respect to the contact angle for fixed permeability ($K = 1.02 \times 10^{-9}$ m^2) is shown in Fig. 11(b). For both cases the base heat transfer coefficient for pyramidal pillars is the highest at any contact angle ($0° < \theta < 60°$).

The variation in the rate of evaporation for different geometries, as presented by the base heat transfer coefficient in Fig. 11, is related to the area of the thin-film region which forms near the contact line. Fig. 12(a) and (b) show the variation of the percentage thin-film area with respect to the contact angle for the different geometries. The percentage thin-film area represents the area of the thin-film region of the meniscus normalized by the combined area of the liquid inlet and the bottom wall. It can be observed from Fig. 12 that the pyramidal pillars possess the largest thin-film area among all the structures. This is true for any contact angle for fixed porosity and fixed permeability. This leads to the higher evaporation rates for pyramidal pillars, as noted from Fig. 11.

4.2.4. Comparison with sintered particle wick structure

The performance of the pyramidal pillars with a porosity of 78% is now compared with that of the sintered particle wick structure with porosities of 78% and 56%. It was discussed earlier that the porosity for the pyramidal pillars cannot be lower than 72% due to geometric constraints and an average porosity of 78% is considered for this comparative study. Commercial sintered particle wick structures have porosities in the 50–70% range [20] and a median porosity of 56% is considered for comparison in this study. The case of 78% porosity for the sintered particle structure is considered to compare the performance of the two structures at a fixed porosity. Porosities of 78% and 56% lead to a pitch of 220 μm and 308 μm, respectively, for square-packed uniform spheres (Fig. 2(d)) with a particle radius of 100 μm. The side length of the pillars is taken as 200 μm. h is taken as being equal to r (100 μm) and $0.2r$ for the particles and pyramidal cases, respectively. Fig. 13(a) presents the variation of the maximum non-dimensional capillary pressure realized in the pyramidal and spherical geometries at different contact angles. It is observed that the pyramidal micropillars lead to a higher capillary pressure than the sintered particle wick structure for the same porosity of 78% ($|\Delta P_c|_{\text{pyramid}} \sim 2.3 \times |\Delta P_c|_{\text{sphere}}$ at $\theta = 5°$). However, the sintered particle structure of the average porosity (56%) generates higher capillary pressure than the pyramidal structure with 78% porosity ($|\Delta P_c|_{\text{sphere}} \sim 2 \times |\Delta P_c|_{\text{pyramid}}$ at $\theta = 5°$).

Table 3 compares the permeability of the sintered particle structure and the pyramidal micropillars. For the fixed porosity case (ε = 78%), the sintered particle wick has a higher permeability than the pyramidal structure while the pyramidal structure is much more permeable than the sintered structure of more typical porosity (ε = 56%).

The base heat transfer coefficient due to evaporation from the liquid meniscus is compared for different contact angles in Fig. 13(b). The solid superheat is taken as 2.5 K while T_{inlet} = 300.5 K and T_v = 298 K. The diameter and side length of the particles and pillars are taken as 200 μm. The liquid level h is taken to be 100 μm for both geometries. For fixed porosity, the evaporation rate is higher in the case of pyramidal pillars than that of the sintered particle structure. However, the sintered particle structure performs better than the pyramidal structure when its porosity is lower (56%).

This comparative study shows that the pyramidal micropillared geometry performs better than the sintered particle structure for the case of fixed porosity (78%). In the case of the average porosity (56%) for sintered particle wick structure, the sintered particle structure leads to the generation of higher capillary pressure and a higher rate of evaporation than the pyramidal structure at 78% porosity. However, the permeability of the micropillared structure is an order of magnitude higher than that of the sintered particle structure. Hence, the pillared structure will lead to smaller liquid pressure drop but a worse performance than the sintered particle structure in terms of wicking and thin-film evaporation. These inferences from the comparative study have been summarized in Table 4. The table shows that micropillars lead to an increase in the capillary limit of the heat pipe or a reduction in the thermal resistance. For applications where a reduction of the liquid pressure drop is of greater concern, the micropillared geometry would be more suitable than the sintered particle wick structure. For thin vapor chambers with very thin wick structures (wick thickness <200 μm) [6], the decrease in the liquid pressure drop is the greater concern in order to avoid dry-out at high heat fluxes. In such cases, the micropillared geometry would be preferred to the sintered particle structure.

5. Conclusions

The wick structure in the evaporator region of a heat pipe determines its thermal performance and maximum heat transport capability. Optimizing the design of the structure is crucial to its operation at high heat fluxes. In this study, numerical models are developed to predict the capillary pressure, permeability and thin film evaporation from liquid menisci formed in the pores of micropillared surfaces. Correlations for the permeability of micropillared structures are proposed as functions of the wick porosity and length scale. The menisci formed in the wick pores of various structures are computed based on a surface energy minimization approach. Evaporation from the meniscus under saturated vapor conditions is calculated using the kinetic theory-based rate of evaporation. Novel structures such as conical and pyramidal pillars are introduced and their performance compared with that of cylindrical pillars. Comparisons are presented for the cases of fixed porosity and fixed permeability. Surfaces with pyramidal micropillars are found to perform best, generating the highest capillary pressure and evaporation rate among all the microstructures considered here. The pyramidal shape of the pillars leads to an increase in the thin-film area near the solid-liquid contact line, thus increasing the rate of evaporation.

The wicking and thin-film evaporation performance of the pyramidal micropillar surface (with porosity of 78%) is also compared with that of a sintered particle wick structure with an average

porosity of 56%. The sintered particle wick structure outperforms the micropillared geometry in terms of the maximum capillary pressure generation and evaporation rate. However, it leads to a significantly higher liquid pressure drop in the wick structure. From the analysis, it is concluded that the thermal performance and the maximum heat transport capability of thin vapor chambers, where large liquid pressure drop at high heat fluxes is of significant concern, can be enhanced by using the micropillared wicks considered in this study.

References

[1] P.D. Dunn, D.A. Reay, The heat pipe, Phys. Technol. 4 (3) (1973) 187.
[2] M.T. North, C.T. Avedisian, Heat pipes for cooling high flux/high power semiconductor chips, J. Electr. Packaging 115 (1) (1993) 112.
[3] R. Ranjan, J.Y. Murthy, S.V. Garimella, Analysis of the wicking and thin-film evaporation characteristics of wick microstructures, ASME J. Heat Transfer 131 (10) (2009) 101001.
[4] J.A. Weibel, S.V. Garimella, M.T. North, Characterization of evaporation and boiling from sintered powder wicks fed by capillary action, Int. J. Heat Mass Transfer 53 (19–20) (2010) 4204–4215.
[5] D.H. Altman, J.R. Wasniewski, M.T. North, S.S. Kim, T.S. Fisher, Development of micro/nano engineered wick-based passive heat spreaders for thermal management of high power electronic devices, in: Proceedings of the ASME 2011 InterPACK Portland, OR, July 6–8 (2011) InterPACK2011-521122.
[6] R. Ranjan, J.Y. Murthy, S.V. Garimella, D.H. Altman, An experimentally validated model for transport in thin, high thermal conductivity, low CTE heat spreaders, in: Proceedings of the ASME 2011 InterPACK Portland, OR, July 6–8 (2011) InterPACK 2011-56039.
[7] R. Ranjan, J.Y. Murthy, S.V. Garimella, A microscale model for thin-film evaporation in capillary wick structures, Int. J. Heat Mass Transfer 54 (1–3) (2011) 169–179.
[8] R. Ranjan, J.Y. Murthy, S.V. Garimella, U. Vadakkan, A numerical model for transport in flat heat pipes considering wick microstructure effects, Int. J. Heat Mass Transfer 54 (1–3) (2011) 153–168.
[9] R. Ranjan, S.V. Garimella, J.Y. Murthy, K. Yazawa, Assessment of nanostructured capillary wicks for passive, two-phase heat transport, Nanoscale Microscale Thermophys. Eng. 15 (3) (2011) 179–194.
[10] P.C. Wayner Jr., Intermolecular forces in change of phase heat transfer: 1998 Donald Q. Kern award review, AIChE J. 45 (1999) 2055–2068.
[11] H.K. Dhavaleswarapu, C.P. Migliaccio, S.V. Garimella, J.Y. Murthy, Experimental investigation of evaporation from low-contact-angle sessile droplets, Langmuir 26 (2) (2010) 880–888.
[12] N.J. Gernert, J. Toth, J. Hartenstine, 100 W/cm^2 and higher heat flux dissipation using heat pipes, in: 13th International Heat Pipe Conference (13th IHPC), Shanghai, China, September 21–25, 2004.
[13] C. Ding, C.D. Meinhart, N.C. MacDonald, Surface modifications of bulk micromachined titanium pillar arrays – a wicking material for thin flat heat pipes, in: Proceedings of the ASME Micro/Nanoscale Heat and Mass Transfer International Conference 2009, Dec. 18–21, 2010, vol. 2, 2010, pp. 415–419.
[14] Y. Nam, S. Sharratt, C. Byon, S.J. Kim, Y.S. Ju, Fabrication and characterization of the capillary performance of superhydrophilic Cu micropost arrays, J. Microelectromech. Syst. 19 (3) (2010) 581–588.
[15] R. Xiao, R. Enright, E.N. Wang, Prediction and optimization of liquid propagation in micropillar arrays, Langmuir 26 (19) (2010) 15070–15075.
[16] H.H. Cui, K.M. Lim, Pillar array microtraps with negative dielectrophoresis, Langmuir 25 (6) (2009) 3336.
[17] S. Nagrath, L.V. Sequist, S. Maheswaran, D.W. Bell, D. Irimia, L. Ulkus, M.R. Smith, E.L. Kwak, S. Digumarthy, A. Muzikansky, P. Ryan, U.J. Balis, R.G. Tompkins, D.A. Haber, M. Toner, Isolation of rare circulating tumor cells in cancer patients by microchip technology, Nature 450 (7173) (2007) 1235.
[18] A.A. Saha, S.K. Mitra, M. Tweedie, S. Roy, J. McLaughlin, Experimental and numerical investigation of capillary flow in SU8 and PDMS microchannels with integrated pillars, Microfluidics Nanofluidics 7 (2009) 451–465.
[19] K.A. Brakke, The surface evolver, Exp. Math. 1 (2) (1992) 141–165.
[20] B.D. Iverson, T.W. Davis, S.V. Garimella, M.T. North, S.S. Kang, Heat and mass transport in heat pipe wick structures, J. Thermophys. Heat Transfer 21 (2) (2007) 392–404.
[21] R.W. Schrage, A Theoretical Study of Interface Mass Transfer, University Press, New York, Columbia, 1953.
[22] Fluent Inc., Fluent 6.2 User's Guide, 2004.
[23] S. Whitaker, Flow in porous media I: A theoretical derivation of Darcy's Law, Transp. Porous Media 1 (1) (1986) 3–25.
[24] MATLAB a, The Mathworks, Natick, MA USA, 2007.
[25] R. Finn, Capillary surface interfaces, Notices Am. Math. Soc. 46 (7) (1999) 770–781.
[26] Y.A. Cengel, Heat Transfer: A Practical Approach, WCB/McGraw-Hill, 1998.
[27] V.P. Carey, Liquid–Vapor Phase Change Phenomena, Hemisphere Publishing Corp., Washington, DC.